ADVANCED OPTICAL MATERIALS
www.advopticalmat.de

Effect of Chlorine Inclusion in Wide Band Gap $FAPbBr_3$ Perovskites

*Daniel Ory, Giuseppe Ammirati, Barbara Paci, Philippe Baranek, Amanda Generosi, Olivier Fournier, Stefano Turchini, Francesco Toschi, Jean-François Guillemoles, Jessica Barichello, Fabio Matteocci, Aldo Di Carlo, Valeria Milotti, Polina M. Sheverdyaeva, Paolo Moras, Daniele Catone, and Stefania Cacovich**

Wide bandgap perovskites have recently gained attention owing to their physical properties, versatility, and potential in various optoelectronic devices including LEDs, detectors, and building-integrated photovoltaics (BIPV). However, BIPV materials must meet conflicting requirements, necessitating high performance, high transparency in the visible spectrum and color neutrality. This study investigates the controlled addition of chlorine in $FAPb(Br_{1-x}Cl_x)_3$ perovskites to achieve band gaps exceeding 2.4 eV. Increasing chlorine content from $x_{Cl} = 0.00$ to $x_{Cl} = 0.25$ widens the band gap from 2.37 to 2.52 eV, effectively improving the visible light transparency. Advanced characterization techniques including X-ray diffraction, synchrotron radiation photoelectron spectroscopy, photoluminescence imaging, and fast transient absorption spectroscopy, complemented by density functional theory, reveal insights into absorption properties, electronic structure, and ultrafast recombination dynamics as a function of the thin film chemical composition. Furthermore, this study evaluates energetic disorder, carrier recombination rates, and non-radiative losses for different compositions by extracting quantitative parameters such as Urbach energy and quasi-Fermi level splitting, offering novel insights and guidelines for the design and optimization of emerging photovoltaic (PV) materials. Optimal PV performance metrics are achieved with a wide bandgap bromine perovskite containing 14% chlorine, striking a balance between morphology, transparency, and voltage losses.

1. Introduction

Compositional engineering stands as a highly promising strategy for enhancing the stability and performance of halide perovskite-based devices.[1,2] Furthermore, the tunability of halide perovskite materials enables the fine-tuning of their optical characteristics to target specific applications,[3] such as tandem solar cells[4,5] or laser systems.[6] Notably, extensive research has been conducted to investigate the influence of chlorine incorporation in methylammonium lead iodide (MAPI), yielding substantial enhancements in optoelectronic and charge transport properties.[7–9] Thin films of $MAPbBr_{3-x}Cl_x$ demonstrate significantly extended recombination lifetimes, a characteristic precisely tuned through varying chlorine concentrations.[10–12] Moreover, methylammonium chloride (MACl) is a commonly used bulk additive in perovskite solar cells.[13–15]

Recently, wide band gap perovskite materials have shown considerable potential in the field of semi-transparent PV applications.[16–19] Additionally, they can

D. Ory, P. Baranek
EDF R&D, EDF Lab Paris-Saclay
Department SYSTEME
Palaiseau 91120, France

D. Ory, P. Baranek
IPVF
Institut Photovoltaïque d'Ile-de-France
Palaiseau 91120, France

The ORCID identification number(s) for the author(s) of this article can be found under https://doi.org/10.1002/adom.202401212

DOI: 10.1002/adom.202401212

G. Ammirati, B. Paci, A. Generosi, S. Turchini, F. Toschi, J. Barichello, A. D. Carlo, D. Catone
CNR–Istituto di Struttura della Materia (CNR–ISM)
Via del Fosso del Cavaliere 100
Rome 00133, Italy

G. Ammirati, F. Matteocci, A. D. Carlo
CHOSE
University of Rome "Tor Vergata"
Rome 00133, Italy

O. Fournier, J.-F. Guillemoles, S. Cacovich
Institut Photovoltaïque d'Ile-de-France (IPVF)
UMR 9006
CNRS
Ecole Polytechnique
IP Paris
Chimie Paristech
PSL
Palaiseau 91120, France
E-mail: stefania.cacovich@cnrs.fr

be employed in light-emitting diodes (LEDs)[20] and photodetector devices,[21,22] as the introduction of chlorine into methylammonium lead bromide ($MAPbBr_3$) enables precise control over emission color and response spectrum. The effects of the incorporation of chlorine in $MAPbBr_3$ systems on their properties were explored by Comin et al., who showed the evolution of the electronic structure of wide-bandgap mixed halide perovskite thin film as a function of Br/Cl substitution.[23] Chlorine incorporation not only impacts the physical properties of the absorber but also affects its stability, by partially suppressing bromide ion migration and increasing charge carrier transport.[24] Furthermore, a combined theoretical and experimental investigation has proven that stability is notably improved when 12–18% of chlorine is incorporated.[25] However, higher concentrations of chlorine result in less stable materials.[25] The use of these absorbers in solar cells or modules has already been proved, leading to champion device efficiency of 6.3% with an average visible transmittance (AVT) of 69.4% for a chloride molar ratio equal to 0.13.[26] In perovskite materials, it is noteworthy that not only the anionic halides can be replaced, but also the cations within the crystal lattice. For instance, perovskite materials based on formamidinium (FA) have demonstrated superior stability when compared to their methylammonium (MA) counterparts, both from an optical perspective[27] and in terms of mechanical properties.[28] Moreover, Br vacancies and interstitials have lower formation energies and higher density in $MAPbBr_3$ as compared to $FAPbBr_3$ single crystals.[29] $FAPbBr_3$ has also been proved to be more resistant to high temperatures and to show self-healing properties when exposed to irradiation,[30] making it a suitable candidate also for applications such as X-ray detectors[31] and space-based technologies.[32]

Despite the extensive literature on the fundamental properties of mixed halide perovskite, an exhaustive and systematic investigation of the effect of chlorine inclusion in $FAPbBr_3$ perovskite thin films is still missing. Such a study is essential for the optimization of the design of optoelectronic devices based on wide-bandgap perovskite materials. In this work, we investigate wide-bandgap mixed halide perovskite materials that leverage the beneficial effects resulting from chlorine incorporation and the utilization of FA cations. Specifically, we conduct a comprehensive investigation of the structural, optical and electronic properties of $FAPb(Br_{1-x}Cl_x)_3$ thin films. We employ a combination of advanced characterization techniques, including X-ray diffraction (XRD), synchrotron radiation photoelectron spectroscopy (PES), photoluminescence (PL) hyperspectral imaging, and fast transient absorption spectroscopy (FTAS) in conjunction with density functional theory (DFT) calculations, to analyze the evolution of key physical and structural parameters as a function of the chlorine content within the range $x_{Cl} = 0.0$ to 0.25. We compared the energy gap (E_g) values obtained using different techniques and constructed the energy band diagram for all compositions. Importantly, this work also provides valuable guidelines for the design of semi-transparent PV systems. This is achieved by quantifying non-radiative losses within various mixed Br/Cl perovskite compositions and evaluating the evolution of critical parameters, including AVT and color rendering index (CRI) with increasing chlorine percentage. We established that the optimal composition is found in wide-bandgap bromine perovskites with a chlorine content of 14%. Such mixed systems indeed offer the best balance between transparency and absorber efficiency. These insights are crucial for the purpose of designing absorbers and solar cells intended for integration into building structures.

V. Milotti, P. M. Sheverdyaeva, P. Moras
CNR–Istituto di Struttura della Materia (CNR-ISM)
SS 14, Km 163,5, Trieste 34149, Italy

2. Results and Discussion

2.1. Theoretical Description and Structural Properties of the Materials

First, our investigation focuses on exploring the structural properties of polycrystalline thin films of $FAPb(Br_{1-x}Cl_x)_3$, where x_{Cl} equals 0, 0.14, 0.19 and 0.25. To achieve this, a combined approach utilizing DFT calculations and experimental XRD measurements was employed.

A hybrid functional was used and optimized to yield an accurate description of the structural, electronic (band gap) and dynamic properties of this family of perovskites. This optimization has been realized with the tetragonal *P4/mbm* phase of $FAPbX_3$ (X = Cl, Br and I), as described in **Figure 1a** (primitive cell) and in Figure 1b (octahedral network). This specific phase description allows us to reproduce the experimentally observed octahedral network reported by Alexandra Franz et al. using neutron diffraction.[33] For $FAPb(Br/Cl)_3$, the Hamiltonian combines 5.625% of exact exchange from Hartree-Fock with PBE exchange-correlation functional.[34] Moreover, it provides results consistent with the experiment and with a more homogeneous qualitative and quantitative description of their properties than the most sophisticated methods based on the GW approximation.[35] This is supported by the comparative analysis shown in Table S1 (Supporting Information). The average errors with respect to the experimental data dispersion in the values of the lattice parameter and band gaps are 2% (± 1%) and 3% (± 2%), respectively (see Table S1, Supporting Information), as it will be illustrated later on.

Then, to investigate the effect of the chlorine substitution on the structural and electronic properties of $FAPbBr_3$, a supercell approach was used. In particular, we focus on the percentage of chlorine going from $x_{Cl} = 0.08$ to 0.25. Regardless of the Cl rate, the Cl distribution does not significantly impact the maximum total inner energy difference between each configuration. This difference remains relatively small, approximately in the order of 0.05 eV. The different configurations have thus the same formation energy within 5E-3 eV per atom. This means that the material is a solid solution composed of a random distribution of chlorides.

The general trend is that the band gap of the substituted compounds increases with the increase of the Cl rate as the lattice parameters decrease. The most stable configurations for the tetragonal symmetry correspond to the $1 \times 1 \times 2$ supercells described in Figure 1c where chlorines occupy the axial positions for $x_{Cl} = 0.16$ chlorine composition. The crystal structures for $x_{Cl} = 0.08$ and 0.25 compositions are reported in the (Figure S3, Supporting Information). Importantly, the spatial chlorine repartition has a direct influence on the bandgap and lattice parameters of the

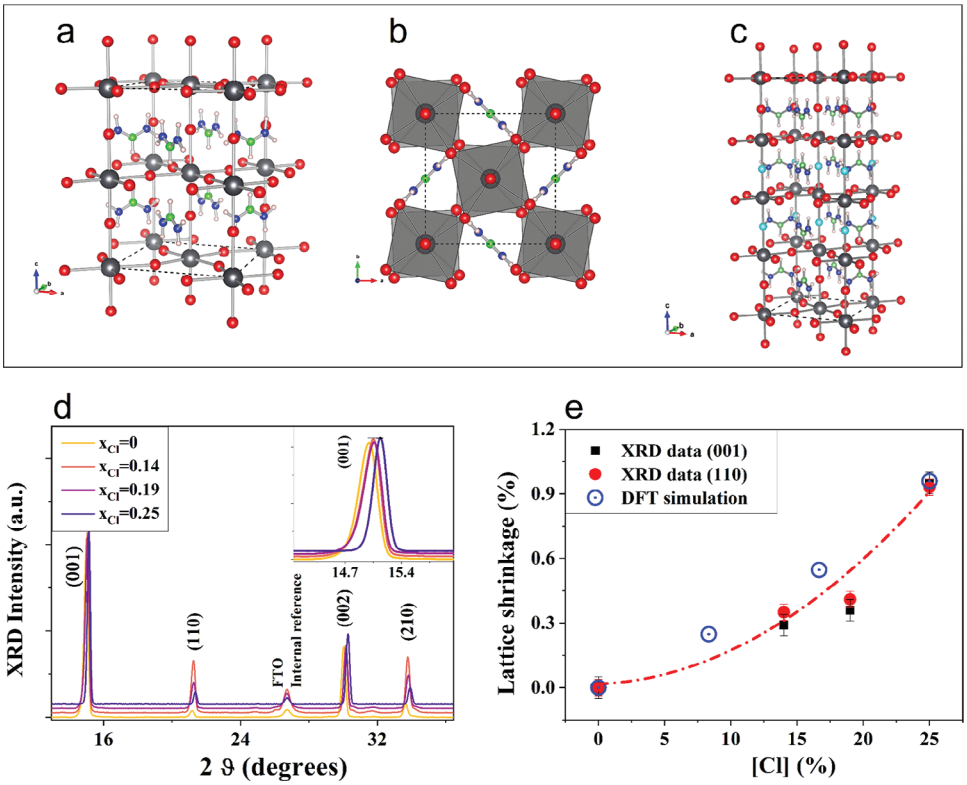

Figure 1. Tetragonal P4/mbm crystal structure of $FAPbX_3$ (X = Cl and Br) used in this work: a) primitive cell; b) octahedral network of this phase. The dashed lines show the lattice cell. Pb, I, C, N and H are in gray, red, green, blue and white, respectively. c) Tetragonal substituted crystal structure of $FAPb(Cl_xBr_{(1-x)})_3$ ($0.08 < x < 0.25$) obtained in this work: the most stable configuration for the $x_{Cl} = 0.16$ of bromine substitution by chlorine (Cl in cyan). d) XRD pattern of the reference perovskite sample compared to patterns collected on samples with different chlorine contents. Miller indexes of the α-phase $FAPbBr_3$ are reported and the FTO substrate is labeled. In the inset, a highlight of the perovskite (001) reflection is reported for all examined samples. e) Lattice shrinkage (lattice parameter relative change) of α-$FAPbBr_3$ as a function of chlorine concentration as deduced by Gaussian fitting procedure of each reflection of the XRD patterns and the results of DFT calculation for $x_{Cl} = 0$, 0.08, 0.16 and 0.25, the dotted line is a guide for the eye.

obtained compound. The range of dispersion of the bandgap is 0.02, 0.14, and 0.15 eV for the $x_{Cl} = 0.08$, 0.16, and 0.25 chlorine content, respectively. The lowest relative variation in terms of lattice parameters was obtained for the configuration with the lowest bandgap and, therefore with the lowest percentage of chlorine. This configuration involves a complete substitution of the axial sites of the Br octahedra by Cl. Conversely, the configurations with the highest bandgap, which corresponds to the substitution of the equatorial sites of the bromine octahedra by chlorine possess intermediate variation of the lattice parameter. The structures exhibiting the most stable configuration correspond to the structure with the highest variation of lattice parameter induced by a partial substitution of the axial Br by Cl (see Figure 1c for an example of axial distribution).

A systematic study was then performed on formamidinium lead bromide perovskites addressing the structural/morphological properties as a function of chlorine content ($x_{Cl} = 0.14$, 0.19 and 0.25) in comparison to a reference sample without any chlorine. XRD was used to monitor the structural properties of the components constituting the samples and to address any modifications induced by chlorine addition. In Figure S4 (Supporting Information), the XRD pattern of the reference sample (glass/FTO (fluorine-doped tin oxide)/$FAPbBr_3$) is reported: the FTO reflections are visible as expected and are labeled according to the theoretical ICDD card nr: 00-001-0657. In addition, Miller indexes are reported for the perovskite signals, perfectly matching an α-$FAPbBr_3$ structure. No spurious contributions are detected.

The same experimental procedure was adopted to observe the structural characteristics of the different perovskite films as a function of chlorine content, and the comparative results are reported in Figure 1d, where the region $\approx 2\vartheta = 15°$ is highlighted in the inset. The FTO substrate is always visible and can be used as an internal absolute reference to evaluate the effect of chlorine addition. Despite the introduction of chlorine into the lattice, the perovskite sample retains the α-$FAPbBr_3$ phase. However, the (001) perovskite reflection highlighted in Figure 1d shifts toward higher 2ϑ values (smaller values of the lattice parameter d) as the chlorine concentration increases.

Table 1 illustrates the modifications of the lattice parameters resulting from the bromine substitution by chlorine. The results obtained by DFT expressed in a pseudo-cubic structure reference frame are in good agreement with the XRD experimental data. The relative difference between the calculated and experimental values is in order of 3% for $x_{Cl} = 0.08$ and 0.25 chlorine concentration. The lattice parameters decrease with the incorporation of the chlorine which possesses a smaller ionic radius than bromine.

Table 1. Calculated isotropic lattice parameters (in Å) for different chlorine concentrations compared to the experimental lattice parameters obtained in this work.

x_{Cl}	DFT simulations	XRD data
0.00	6.091	5.907
0.08	6.0762	
0.14		5.890
0.16	6.058	
0.19		5.886
0.25	6.033	5.851

The analysis of the variation of the lattice parameters of the α-$FAPbBr_3$ as a function of chlorine concentration, as deduced from the Gaussian fitting procedure of each reflection of the XRD patterns, are reported in Figure 1e together with the results of DFT simulation. The quantitative analysis of individual perovskite reflection displays a variation in the relative lattice parameter values as a function of chlorine concentration. In Figure 1e, the % of lattice parameter variation ($\Delta d/d$) as a function of chlorine addition, is shown for two crystallographic orientations (001 and 110) representative of all orientations. The computational findings obtained through DFT demonstrate a close correspondence with the experimental data.

Subsequently atomic force microscopy (AFM) investigation was performed on the aforementioned samples to evaluate the effect of chlorine on the topography of those films.

Indeed, since the perovskite layer represents the active material of the integrated complete device, its morphology is also very important when the fabrication of the PV cell is to be considered: controlling the morphology at the interface of the different layers composing the device is actually a critical issue, among the different structural/physical/chemical properties affecting the final efficiency. Therefore, here, the effect of chlorine addition on the perovskite film topography was considered to keep under control its effect on the active layer/transport layer interface. In Figure S5 (Supporting Information) 10*10 µm AFM images representative of the whole surface of the various films are reported and additional AFM images of different dimensions are reported in Figures S6–S9 (Supporting Information).

The statistical analysis of the surface roughness indicates that the topography is influenced by the addition of chlorine. Indeed, the thin films exhibit reduced homogeneity for higher chlorine concentrations, with roughness values ranging from 26 nm in the case of $x_{Cl} = 0$ to 60 nm for $x_{Cl} = 0.25$, as reported in Figure S5 (Supporting Information) showing the root mean square (r.m.s) roughness image dimension histograms.

2.2. Surface Composition and Electronic Properties

Synchrotron radiation PES was used to study the chemical composition and valence band structure of the $FAPb(Br_{1-x}Cl_x)_3$ perovskites. PES survey spectra acquired at $h\nu = 750$ eV on as-received samples (Figure S10, Supporting Information) display all expected core level peaks (N 1s, C 1s, Cl 2p, Br 3p, Pb 4f, Br 3d), along with signatures of surface contamination (O 1s and the C 1s component at 284.7 eV ascribed to adventitious carbon). The experimental stoichiometry of the perovskites (specifically the Cl content with respect to the Br content) can be obtained from the areas of the peaks, normalized to the respective photoemission cross sections at $h\nu = 750$ eV. Figure S11 (Supporting Information) reports spectra and related fittings of the Cl 2p (Cl $2p_{3/2} = 198.1$ eV) and Br 3p (Br $3p_{3/2} = 182.0$ eV) peaks for the as-received samples with nominal Cl content x_{Cl}. From the normalized peak areas (A_{Cl} and A_{Br}, photoemission cross sections $\sigma_{Cl\ 2p} = 0.23$ and $\sigma_{Br\ 3p} = 0.25$[36]) we can derive the experimental chlorine content $x_{exp} = A_{Cl}/(A_{Cl} + A_{Br})$. By comparing nominal and experimental values (x = 0.14/0.19/0.25; x_{exp} = 0.17/0.19/0.29), we notice a maximum absolute discrepancy of 0.04, which indicates a slight excess of chlorine with respect to the target composition. The $FAPb(Br_{1-x}Cl_x)_3$ samples were sputtered for 6 min with Ar^+ ions to remove surface contamination and reveal the genuine electronic structure of the perovskites,[37] in analogy to the procedure used for the recent analysis of $FAPbBr_3$.[30] The core level PES spectra collected on the sputtered samples (Figure S12, Supporting Information) show a further increase of the Cl content (x_{exp} = 0.2/0.22/0.32), probably due to sputtering-induced formation of gaseous Br_2, which easily leaves the sample surface.[30] **Figure 2a,b** report exemplary spectra and fittings of the Cl 2p to Br 3p peaks after sputtering for $x_{Cl} = 0$ and $x_{Cl} = 0.25$, respectively.

The valence band energy region (0–7 eV of binding energy) was explored for all the samples by using 75 eV of photon energy. In Figure 2d the PES spectrum of $x_{cl} = 0.25$ shows three distinct peaks which are fitted with three gaussians (P1 in red, P2 in green, and P3 in blue), while a Shirley function accounts for the background. All the investigated samples consistently reveal three peaks centered at ≈2.3, 3.5, and 4.6 eV of binding energy. These three features are assigned to the first three valence bands in agreement with the electronic structure predicted by DFT calculations. The partial density of states (pDOS) of Br 4p and Cl 3p (Figure 2e) and of Pb 6s and Pb 6p (Figure 2f) was rigidly shifted by 0.95 eV to be aligned with the experimental spectrum, a method well established in the literature.[38] This comparison indicates that the P1 feature is primarily influenced by Br 4p, whereas P2 and P3 stem from a combination of Br 4p and Cl 3p, with a minor contribution from Pb 6s and 6p states.

The PES spectra were also employed to evaluate the valence band (VB) edge, by estimating the onset of the signal by a linear extrapolation and identifying the intersection between the background and the signal (Figure 2c). Notably, this parameter exhibits a consistent linear increase with the chlorine percentage (15 meV/Cl%), as shown in the inset of Figure 2c. These energy values are fundamental in the estimation of the band diagram for the studied materials, as discussed later in the text.

2.3. Steady-State Optical Properties

We investigated the optical characteristics of the mixed perovskite layers through a systematic approach. First, we performed reflectance (R) and transmittance (T) measurements to characterize their absorption properties. Then, we employed absolutely calibrated hyperspectral photoluminescence imaging analysis to locally assess and quantitatively evaluate the opto-electronic properties of the thin films. The transmission curves for all the tested compositions are shown in **Figure 3a**, together with the human

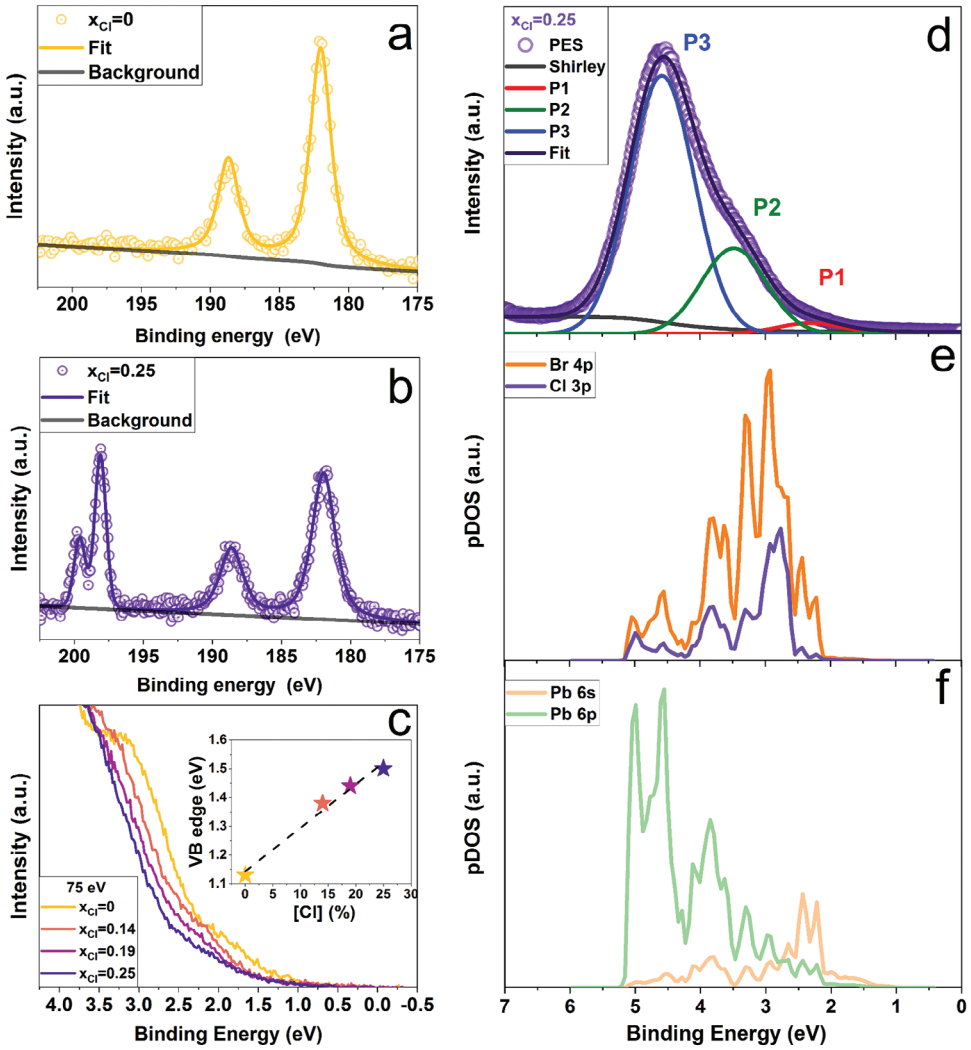

Figure 2. a,b) PES spectra ($h\nu$ = 750 eV) and fittings of the Cl 2p to Br 3p peaks of sputtered $FAPb(Br_{1-x}Cl_x)_3$ perovskites with nominal Cl content x_{Cl} = 0 and 0.25. The energy step of the spectra is 200 meV in (a) and 25 meV in (b). c): Photoelectron spectra acquired at 75 eV for $FAPbBr_3$, and chlorine content of x_{Cl} = 0.14, 0.19 and 0.25 in the range of 0–3.5 eV of binding energy. The inset shows the energy values of the onset of the first VB, together with the best linear fit. d): Experimental photoelectron spectra of the film of x_{Cl} = 0.25 acquired at 75 eV of photon energy (black scatter) and the close fitting of the peak P1 (orange line), P2 (green line), and P3 (blue line) and the Shirley background (grey line). e,f) represent the projected DOS for the states contributing to the top of the VB and associated to the p orbitals of Br and Cl, and, the 6s and 6p orbitals of Pb, respectively.

photopic response (sensitivity) in gray. We can note that the overlap of the eye sensitivity curve decreases when the chlorine content rises, indicating a better visible transmission. In Figure 3b the data depicted show two important parameters for Building-Integrated Photovoltaics (BIPV): AVT and CRI. It should be underlined that CRI and AVT are strongly correlated. AVT is relevant for the evaluation of the perceived transparency by human people and represents the transmission weighted by the eye photonic response and the solar photon flux. CRI is an index measuring the ability of a light source to reveal the colors of objects in contrast to a natural light source. From x_{Cl} = 0.14 to 0.19, the increase in AVT is almost linear and then barely increases from x_{Cl} = 0.19 to x_{Cl} = 0.25, for which it reaches ≈70%. The Color Rendering Index is a complex calculation and helps to qualify the color neutrality with a higher index indicating superior fidelity in reproducing the true colors of an object. A CRI value above 80% and up to 90% corresponds to an acceptable to good color neutrality.[39,40] The CRI increases significantly when the chlorine content increases from x_{Cl} = 0 (CRI = 40.4%) to x_{Cl} = 0.25 reaching a value of 65.2%, a value still below neutral influence on color rendering. Actually, the sample is still yellowish, as shown in Figure S1 (Supporting Information). Assuming a linear increase of CRI and AVT with chlorine content, we can estimate that a chlorine content x_{Cl} = 0.40 would be necessary to reach 80% of CRI and 81% for AVT. Thus far, the increase in chlorine content seems beneficial to the visible properties of this kind of wide bandgap perovskite. Nevertheless, as evidenced in Figure S5 (Supporting Information), the samples do not present the same roughness, exhibiting higher values in the case of x_{Cl} = 0.25, which might have slightly affected the visible properties of the thin films.

The absorption coefficient curve for x_{Cl} = 0 is shown in Figure 3c, while the curves for the other composition can be

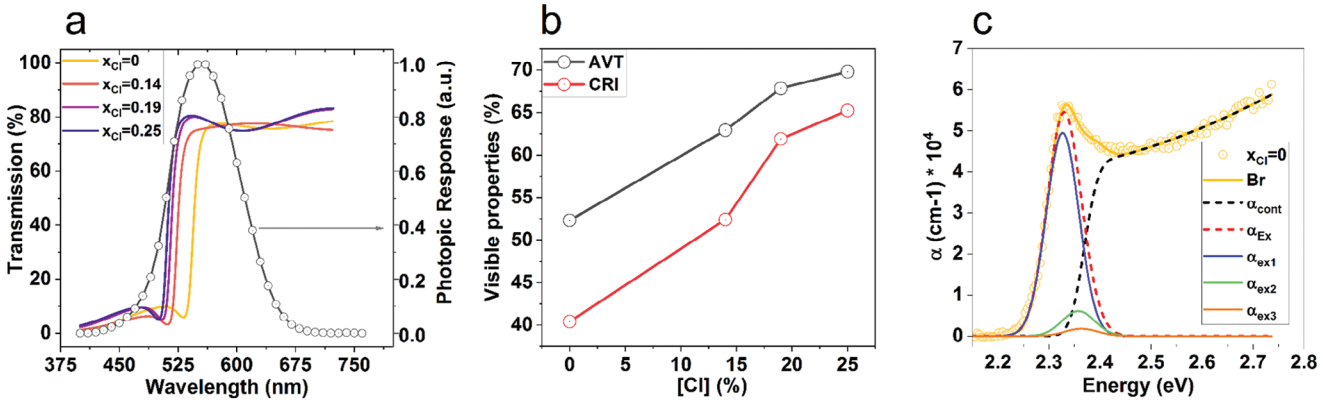

Figure 3. a) Transmission curves for $FAPb(Br_{1-x}Cl_x)_3$ with x_{Cl} ranging from $x_{Cl} = 0$ to $x_{Cl} = 0.25$ and human photopic response in grey. b) AVT and CRI for all compositions. c) Absorption coefficient curve for $FAPbBr_3$, with Elliott fit (orange) and its continuous (dotted black) and excitonic contribution (dotted red). The components of the latter are continuous lines of blue, green and orange. The fitting curves for the other compositions are reported in Supporting Information.

found in Figure S18 (Supporting Information). The basis for absorption modeling by excitons is the work of Elliott.[41] Several further works propose similar but different formulas regarding the application of this model to perovskite analysis.[42–46] All of them are based on the sum of α_{Exc} the contribution of exciton bound states with quantized energy levels "n" and α_{Cont} the contribution of the band-to-band transition, as in the following equation:

$$\alpha_{Elliott}(E) = \alpha_{Cont} + \alpha_{Exc} \quad (1)$$

We calculated the excitonic peak α_{EX} as the sum of the first three bands, with the higher-order bands being neglected. Fitted curves for the different excitonic peaks and continuous components were obtained by using the exciton absorption modeling described below with Equations (2) to (3), where E is the energy of the photon and $x = \sqrt{(R_{exc}/(E - E_g))}$:

$$\alpha_{Exc} = \sum_n \alpha_{E_{x,n}}(E) = A_{exc} \sum_n \left(\frac{1}{E} \frac{4\pi R_{exc}^{\frac{3}{2}}}{n^3} \right) \otimes N\left(E, E_g - \frac{R_{exc}}{n^2}, \sigma_{ex}\right) \quad (2)$$

$$\alpha_{Cont}(E) = A_{cont} \int_{E_g}^{\infty} \left(\frac{1}{E} \frac{\pi \exp(\pi x)}{\sinh(\pi x)} \sqrt{E - E_g} \frac{1}{1 - b\left(E - E_g\right)} \right) \otimes N\left(E - E, 0, \sigma_{cont}\right) dE \quad (3)$$

Both terms include broadening functions N(energy, central energy, broadening factor), such as Gaussian or Lorentzian or Sech distributions, to phenomenologically account for structural or thermal fluctuations of the optical transitions. R_{ex} stands for the exciton binding energy and E_g for the bandgap energy. The crossed circle in Equation (2) stands for the convolution operator.

Two different approaches are reported in the literature, concerning the treatment of amplitude associated with the excitonic or continuous component of absorption, denoted as A_{exc} and A_{cont}, respectively. These amplitudes can be considered equal[44,47,48] or different,[49,50] depending on how physical constants and effective masses are integrated into the global equation.

We choose to consider different effective amplitudes A_{exc} and A_{cont}. The bowing parameter "*b*" introduces a curvature of the continuous part of the absorption at high energy due to the non-parabolicity of the band and provides better fitting of the bending of the absorption curve.[42,44,47,48]

We report in **Table 2** the parameter values obtained from the fit for all mixed compositions. Most of the excitonic properties exhibit a low variation for the explored range of chlorine content. This is confirmed when examining the absorption coefficient curves, which have been normalized and centered to match the pure bromide one. They all appear superimposed within the energy range of the excitonic contribution, as shown in Figure S17 (Supporting Information). Apart from the bandgap, which will be discussed later together with results obtained by other methods, only the amplitudes A_{exc}, A_{cont} and the bowing parameter *b* evolve with the chlorine content. We notice that the higher the chlorine content, the higher the absorption of the perovskite layer, as A_{exc} and A_{cont} increase by almost 50% from $x_{Cl} = 0$ to $x_{Cl} = 0.25$ of chlorine. The ratio A_{exc}/A_{cont} equals 1.12 for the pure bromide content and is ≈1.15 for all chlorine compositions.

The exciton binding energy remained ≈41 meV for all compositions. Such behavior is unexpected as generally this parameter was found to increase with the bandgap.[23] Notably, a similar stability was previously reported for $MAPb(Br_xCl_{1-x})_3$ thin films.[26] However, Comin et al.[23] observed an increase from 21 meV for $x_{Cl} = 0$ to 31 meV for $x_{Cl} = 0.25$. This discrepancy might come from differences in sample processing conditions. In addition, Galkoswski et al.[51] found a value of the binding energy by magneto-transmission measurement equal to 1% of the bandgap, indicating an increase of only 1.5 meV from $x_{cl} = 0$ to $x_{cl} = 0.25$. This minimal variation is compatible with our results. It is worth noting that most of the literature regarding $FAPbBr_3$ and –Cl mixed compositions is based on nano-structures, like quantum dots or nanowires, which exhibit different optical properties compared to thin films, for which limited data can be found. Regarding pure bromide $FAPbBr_3$ thin film, Gen et al. reported a binding energy of 60 meV.[52] Ndione et al.[53] fitted the second derivative of the dielectric function and obtained an

Table 2. Absorption curves fitting parameters evaluated with the Elliott model.

x_{Cl}	E_g (eV)	R_{exc} [meV]	σ_{ex} [meV]	σ_{cont} [meV]	A_{exc} [a.u.]	A_{cont} [a.u.]	b [eV^{-1}]
0.00	2.37	41	32	21	88 000	78 500	0.79
0.14	2.46	41	32	20	118 500	101 500	0.73
0.19	2.50	42	32	19	116 000	100 000	0.70
0.25	2.52	41	32	21	131 000	115 000	0.64

Eg = 2.30 eV and an absorption onset at 2.24 eV, suggesting a binding energy in the order of 30 meV. Theoretical calculation of Jain et al.[54] led to R_{exc} = 22 meV. Therefore, our finding of a binding energy of 41 meV is compatible with the dispersion encountered in the little existing literature for $FAPbBr_3$.

We then acquired absolutely calibrated and spatially resolved PL spectra for all the compositions. The intensity of the acquired photoluminescence data cubes $I_{PL}(x,y,\lambda)$ can be expressed by the generalized Planck's law.[55–57] This law can be applied to the emission of semiconductors that are not in equilibrium and can be expressed by following Equation (4) in the Boltzmann approximation:

$$I_{PL}(E,T) = A(E,T)\ \varphi_{BB}(E,T)\ exp(\Delta\mu/kT) \quad (4)$$

where A is the absorbance of the device, φ_{BB} is the blackbody emission and $\Delta\mu$ stands for the quasi-Fermi levels splitting (QFLS). E is the photon energy, T the temperature, and k is the Boltzmann constant (see Methods section for the description of the absorbance model).

The PL spectra are fitted, either spatially averaged or pixel by pixel, to get different parameter maps. The spatially averaged photoluminescence spectra and the corresponding fits are reported in **Figure** 4a. Additionally, the low energy tail of the absorbance curves $A(E)$ can be used to extract the Urbach energy. The Urbach energy is a phenomenological data representative of the chemical and thermal fluctuations in the material and is related to the voltage loss for thin film absorbers.[44] The Urbach energy (E_u) for all compositions was extracted by fitting the low energy tail of the absorbance obtained from the spatially averaged PL spectra and making use of Equation (4), as shown by the green curve in Figure 4b. The results reveal a slight but continuous and linear increase of E_u from 15.6 meV for x_{Cl} = 0 up to 17 meV for x_{Cl} = 0.25, with a standard error on the fitted results less than ±0.5%. We also fitted the low energy tail of the absorption coefficient curves to extract the same data E_u, represented by the red curve in Figure 4b. In this case, the Urbach energy ranges from 17 meV up to ≈19 meV for x_{Cl} = 0.19 and 0.25 with a higher standard error of ± 3% maximum. The slight decrease by ≈−1% from x_{Cl} = 0.19 to 0.25 is not expected but it is likely within the range of uncertainties associated with sample fabrication, fitting, and measurement. In both cases, the values of E_u are close to each other but statistically different, and importantly, these values are fully compatible with results previously reported, theoretically or experimentally, for organo-metallic perovskite.[43,44,58]

Furthermore, through the use of multi-dimensional PL spectra fitting, we have derived two critical parameters characterizing the optoelectronic properties of thin film semiconductors: the QFLS and the apparent bandgap, representative of the effective optical transition for absorption. The fitting procedure was applied to both average spectra and individual pixels to yield quantitative maps and investigate the degree of uniformity. The resulting maps of apparent bandgap and QFLS for all compositions are illustrated in Figures S19 and S20 (Supporting Information), revealing a good level of uniformity. The spatial dispersion remains consistent across all compositions, approximately at 3.7% for the E_g and 0.45% for the QFLS. Notably, the highest dispersion occurs at x_{Cl} = 0, while the lowest is observed at x_{Cl} = 0.14.

In Figure 4c, the QFLS under one sun illumination (yellow curve) is displayed, obtained by fitting spatially averaged spectra using Equations (4). In addition, a comparison is made with the radiative QFLS ($QFLS_{rad}$) (green curve), serving as a theoretical limit for optical measurements. The $QFLS_{rad}$ is the voltage achievable by a device without non-radiative losses, at both bulk and interfacial levels, operating at one sun illumination. The difference "$QFLS_{rad}$-$QFLS_{1sun}$" is therefore an indicator of the voltage losses due to non-radiative recombination. Notably, starting from x_{Cl} = 0.14, the $QFLS_{1sun}$ reaches a plateau, diverging from the trend of the theoretical limit. This suggests that the quality of the thin films with x_{Cl} = 0.19 and x_{Cl} = 0.25 is lower in terms of their optoelectronic properties, resulting in higher non-radiative losses. Additionally, we investigate the variation of the quantity "E_g-$QFLS_{1sun}$" (red curve), which serves as another indicator of non-radiative losses but also includes absorption properties. The latter quantity is of interest because the PL intensity at the peak scales as the exponential of "E_g-$QFLS_{1sun}$" and is more often reported in literature than "$QFLS_{rad}$-$QFLS_{1sun}$". Both voltage loss indicators show a substantial increase at x_{Cl} = 0.19 and 0.25, evolving with parallel trends. We also calculated the normalized voltage loss "1-$QFLS_{1sun}/E_g$" to mitigate the effect of gap variation when looking at voltage loss. Interestingly, this additional indicator exhibits a minimum for x_{Cl} = 0.14 and a sharp increase for higher chlorine content. The values of all these parameters for the different perovskite compositions are reported in **Table 3**.

Finally, we defined a pseudo-LUE (light utilization efficiency), which is calculated according to Equation (5) from the optical available data and called optical LUE: LUE_{opt}. Figure 4d presents its evolution with chlorine content, normalized to the value for pure bromine composition.

$$LUE_{opt} = AVT * QFLS_{1sun} * J_{SC_{opt}} \quad (5)$$

where $J_{SC_{opt}} = q \int_{energy} A * \phi_{sun}$ in which q is the elemental charge, ϕ_{sun} stands for the solar flux photon density and $A = (1 - T - R)$ is the absorptivity of the layer, with R thereflexion coefficient and T the transmission.

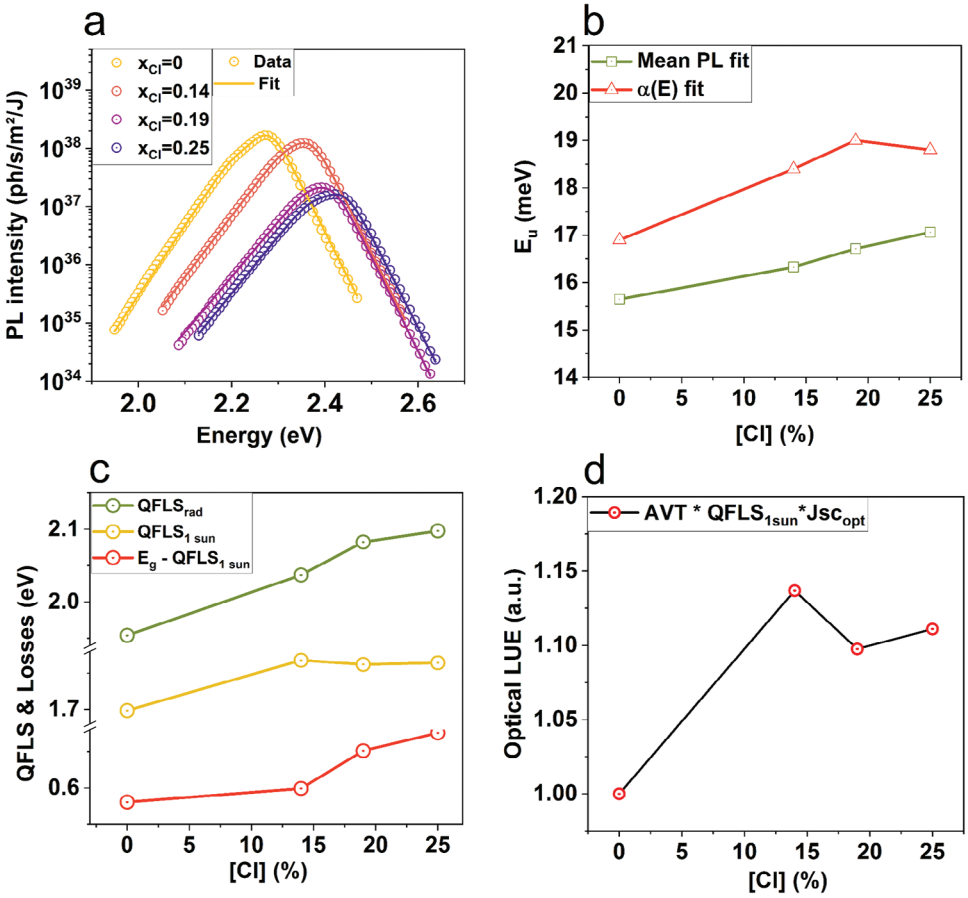

Figure 4. a) Spatially averaged and absolutely calibrated PL spectra for $FAPb(Br_xCl_{1-x})_3$ thin films, with x_{cl} = 0, 0.14, 0.19, and 0.25. b) Estimation of Urbach energy from a fit of the low tail of the absorption curve (red) and from a fit of the low energy tail of PL spectra (green). c) Radiative (green) and measured at one sun equivalent illumination (yellow) quasi-Fermi level splitting values for different chlorine percentages. The difference between the energy gap and quasi-Fermi level splitting at 1 sun, representative of non-radiative voltage losses, is reported in red. d) Optical Light Utilization Efficiency variation, as defined in Equation (5), as a function of perovskite composition, all values normalized to x_{Cl} = 0.

The addition of chlorine demonstrates a clear effect on the optical LUE, as we observe a clear increase starting in this parameter from x_{Cl} = 0.14. This analysis shows that the composition x_{cl} = 0.14 seems to be the most promising absorber in terms of combined visible properties and potential device performance (best optical LUE, layer spatial homogeneity, lowest voltage loss). This result is in line with that of Matteocci et al.[26] whose work concludes that 13% of chlorine incorporated into $MAPbBr_3$ exhibits the best LUE. The optical LUE for the x_{Cl} = 0.25 composition is slightly higher than that for the x_{Cl} = 0.19 composition (1.10 versus 1.11), which is unexpected. We attribute this small difference to minor uncertainties during the fabrication process or measurements. Finally, it is important to note that maximizing power conversion efficiency in a PV device necessitates the consideration of several parameters beyond V_{oc}, such as the short-circuit current and fill factor. Nevertheless, probe device optimization extends beyond the scope of this study. To achieve maximum efficiency, a dedicated investigation is necessary to determine the most suitable transport layer for each composition. Furthermore, additional studies are required to mitigate interfacial recombination processes, which strongly affect the final device performances.

Table 3. Values of radiative $QFLS_{rad}$, one sun equivalent QFLS and voltage losses "E_g-$QFLS_{1sun}$" and "$QFLS_{rad}$-$QFLS_{1sun}$" and normalized voltage loss "1-$QFLS_{1sun}/E_g$".

x_{Cl}	$QFLS_{rad}$ [eV]	$QFLS_{1sun}$ [eV]	E_g–$QFLS_{1sun}$ [meV]	$QFLS_{rad}$–$QFLS_{1sun}$[meV]	1-$QFLS_{1sun}$ [eV]/E_g [a.u.]
0	1.95	1.74	535	210	235
0.14	2.04	1.82	550	220	232
0.19	2.08	1.81	600	270	249
0.25	2.10	1.82	623	280	256

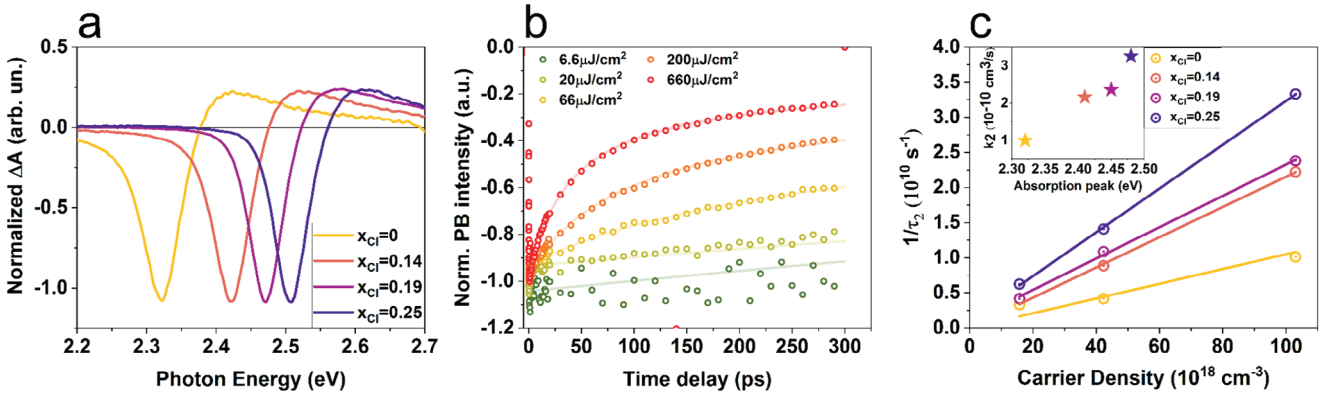

Figure 5. a) Normalized transient spectra obtained at the fixed time delay of 10 ps for x_{Cl} = 0 (yellow), 0.14 (orange), 0.19 (violet), and 0.25 (purple); b) Normalized PB temporal dynamics (scatter) and the relative fitting curve (line) at the pump photon energy of 2.75 eV and the excitation fluences of 6.6 μJ cm^{-2} (green), 20 μJ cm^{-2} (light green), 66 μJ cm^{-2} (yellow), 200 μJ cm^{-2} (orange) and 660 μJ cm^{-2} (red) of x_{Cl} = 0.25; (c) The $1/\tau_2$ values plotted with respect of the carrier density for x_{Cl} = 0, 0.14, 0.19 and 0.25, together with the linear fit used to estimate the values of k_2. Inset: the k_2 values are plotted as a function of the energy of the absorption peaks for studied samples.

2.4. Ultrafast Recombination Dynamics

In this section, we will show the results obtained on the radiative recombination dynamics that last in the first tens of picoseconds after the excitation by means of FTAS, and discuss how these recombination processes are affected by the chlorine content.

Figure 5a reports the normalized transient absorption spectra obtained for x_{Cl} = 0, 0.14, 0.19 and 0.25, which show a negative peak of photo-bleaching (PB) in the energy region of the gap, and a positive peak at higher energies due to photo-induced absorption (PIA) of the probe. The PB and PIA signals are generated by different dynamical processes induced by the excitation of the pump, such as band filling,[59] bandgap renormalization[59] and changes in the refractive index.[59] All the studied samples show transient spectra with similar line shapes but shifted along the energy axis as a function of the chlorine percentage in agreement with the absorption spectra. The energy values of the minimum of the PB signal are reported in **Table** 4 and depicted in **Figure** 6a.

In this context, the charge-carrier dynamics of the mixed-halide perovskites were investigated as a function of the pump fluence with the aim of evaluating how the chlorine content affects the recombination rate of the free carriers. Figure 5b shows the normalized temporal dynamics of the PB peaks of x_{Cl} = 0.25 sample as a function of the fluence of the pump at 2.75 eV (6.6, 20, 66 200 and 660 μJ cm^{-2}). Figure S22 (Supporting Information) reports the normalized temporal dynamics of the other samples in the same experimental conditions. At low fluences (6.6 and 20 μJ cm^{-2}) all samples show a single long-lived decay trend that was assigned to the monomolecular/excitonic recombination. The time constant of this process was estimated to be 2.5 ns for all the materials by fitting the data with an exponential decay function. The dynamics at higher fluences show a more rapid decay trend in the first tens of picoseconds that becomes faster as the pump fluence increases. This contribution is assigned to the second-order radiative bimolecular recombination, which is a process that is enhanced with the increase of the charge-carrier density and hence the pump fluence. The formula used to fit the temporal dynamics is the following:

$$\Delta A\ (t) = \Delta A_1 e^{-\frac{t-t_0}{\tau_1}} + \frac{\Delta A_2}{1+\frac{t-t_0}{\tau_2}} \quad (6)$$

where ΔA_1 is the weight of the monomolecular component, ΔA_2 is the weight of the bimolecular component, τ_1 is the monomolecular time constant, τ_2 is the bimolecular time constant, and t_0 is fixed to 2 ps as the lowest time delay used in the fitting procedure. The bimolecular rate constant k_2 was estimated for all the samples starting from the following formula:

$$\frac{1}{\tau_2} = k_2 n_0 \quad (7)$$

where τ_2 is the time constant estimated by Equation (6) and n_0 is the carrier density calculated for each pump fluence used, (see SI for details). Figure 5c reports the values of $1/\tau_2$ with respect to n_0 for FAPbBr and x_{Cl} = 0.14, 0.19 and 0.25, together with the linear fit used to estimate the values of k_2 in agreement with a bimolecular recombination process. The inset shows the k_2 values plotted as a function of the energy of the absorption peaks of studied samples and reported in Table 4.

These results are consistent with the results of an I-Br mixed composition[60] and show a monotonic increase of the bimolecular recombination rate with increasing the chlorine content. This trend suggests that the change in the composition of the material promotes the electron-hole radiative recombination process. Specifically, the substitution of bromine with chlorine alters the atomic characters of the first valence bands, as evidenced by pDOS calculations (see Figure 2e,f). Additionally, it induces

Table 4. Bimolecular rate constant k2 for x_{Cl} = 0, 0.14, 0.19 and 0.25.

x_{Cl}	k_2 [10^{-10} cm^3/s]
0	1.0 ± 0.2
0.14	2.16 ± 0.06
0.19	2.36 ± 0.07
0.25	3.26 ± 0.07

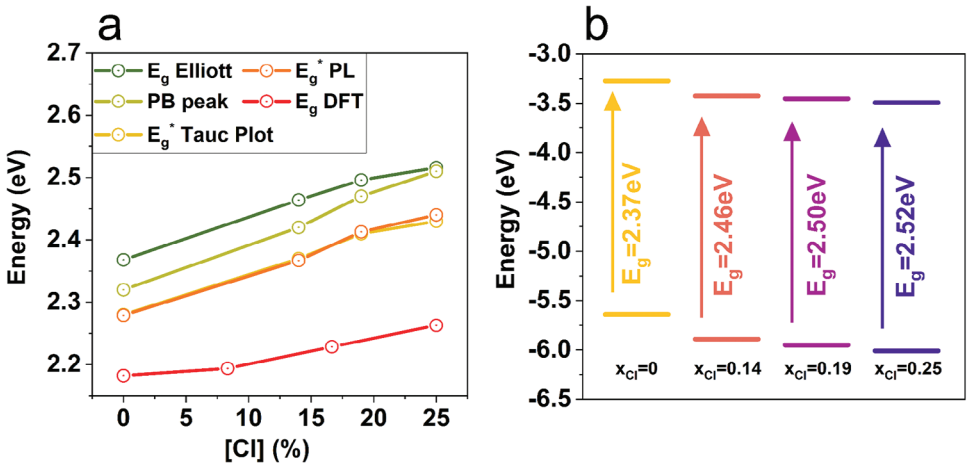

Figure 6. a) Evolution of optical transition versus chlorine content obtained with various methods: Elliott fit, photo-bleaching (PB) peak, Tauc plot, photoluminescence spectra and DFT simulation. b) Schematic diagram of the valence band and conduction band energies with respect to the vacuum level together with the electronic band gap estimated with Elliott fit for all the investigated materials.

a compression of the crystal lattice, as reported by XRD results and DFT simulations (see Figure 1). All these factors contribute to facilitating the bimolecular recombination, leading to a higher k_2 value.[61] This trend suggests that under PV conditions, the carrier lifetime falls within the microsecond time regime, indicating the $x_{Cl} = 0.25$ as the material with the shorter radiative carrier lifetime. This parameter should be considered in the design of a semi-transparent PV device because it represents the upper limit for the temporal window of the charge extraction that is also strongly influenced by the thickness of the film, the band alignment of the transport materials and the non-radiative recombinations.

3. Discussion

In Figure 6a are depicted the energy values of the optical transitions obtained by using different approaches, previously described in this work. Specifically, we report and compare the results obtained by DFT calculations, Tauc plot, spatially averaged PL spectra, Photo-Bleaching peak and Elliott fit. All values are also reported in **Table 5**. The optical transitions derived through the application of the Elliott formula are the one representative of the actual bandgap of the material, noted as E_g. We will call the others "pseudo-bandgap", noted as E_g^*, as they correspond to the energy position of the optical transition involved in the absorption process, including the excitonic contribution. When considering the evolution of bandgap or pseudo-bandgap in relation to the content of chlorine, all the different methods exhibit very similar slopes, giving a consistent picture of the effect of chlorine incorporation. As expected, the bromide-by-chloride substitution widens the bandgap of $FAPbBr_3$. Interestingly, the pseudo-bandgap obtained by the PL fit closely aligns with the one obtained by the Tauc plot fit, confirming these values as the most probable from a practical absorption-emission point of view. The bandgap obtained by Elliott fit is higher by 88 meV on average, as it corresponds to the continuous part of the absorption coefficient according to Elliott's theory. DFT calculations are in reasonable agreement with the experimental values as the error between both does not exceed 3%. The difference in absolute values shown by the FTAS data is due to the fact that the derivative-like shape of the transient response for this class of materials is more influenced by the bleaching of the excitonic resonance rather than by the electronic gap.[62] For this reason, the shift of the PB follows the shift of the excitonic peak in the absorption spectrum that was principally influenced by the increase of the band gap.

Table 5. Energy values of all the data depicted in Figure 6a obtained for $FAPbBr_3$ and $x_{Cl} = 0.14$, $x_{Cl} = 0.19$, and $x_{Cl} = 0.25$ samples, and also $x_{Cl} = 0.08$ and $x_{Cl} = 0.16$ for DFT results.

x_{Cl}	E_g Elliot Fit [eV]	PB peak [eV]	E_g^* PL [eV]	E_g^* Tauc Plot [eV]	E_g DFT [eV]
0	2.37	2.32	2.28	2.28	2.18
0.083					2.19
0.14	2.46	2.42	2.37	2.37	
0.166					2.23
0.19	2.50	2.47	2.41	2.41	
0.25	2.52	2.51	2.44	2.43	2.26

To our knowledge, literature does not report bandgap data for mixed bromine-chlorine compositions based on FA, but only for pure bromine $FAPbBr_3$. The reported values are also generally pseudo-bandgap only. We found it equal to 2.28 eV for $FAPbBr_3$, when Mannino et al.[63] found 2.27 eV by Tauc plot fit, but 2.30 eV with the second derivative of dielectric function. With the same latter method, Ndione et al[53] report 2.30 eV and Feng et al.[64] 2.31 eV with Tauc plot fit. These experimental values are consistent with ours.

Then, we estimated the conduction band energy position by adding the bandgap from Elliott fit to the valence band energy data provided by our PES experiment. Both band data are shown in Figure 6b, together with the real bandgap values obtained by the Elliott fitting method. The valence band energy position decreases with chlorine content by −15 meV/%, which, added to the slope of the bandgap, implies a slope of −9 meV/% for the

conduction band energy. As it was shown previously, the major part of the upper valence bands near the gap of 2.3 eV consist mainly of the p orbitals of Cl and Br which hybridize with the p orbital of Pb. The lower states of the conduction bands are mainly composed of empty s orbitals of Pb. The increase in the band gap is therefore mainly due to the shift toward lower energies of the top of valence bands due to the increasing contribution of the p chlorine's orbitals to these bands.

In this work, we quantified the potential performance of full PV devices for the different compositions on the basis of the quasi-Fermi level splitting and voltage loss analysis, as reported in Figure 4c,d. The trend of the voltage loss is similar to the evolution of Urbach energy (Figure 4b) as well as that of the lattice parameter shrinkage (Figure 1e) and surface roughness (Figure S5, Supporting Information) when chlorine content increases. The observed correlation between Urbach energy and lattice parameter variation has been previously reported in various studies, particularly in the context of perovskite thin films.[65,66] However, this correlation extends beyond halide perovskites, as evidenced by relevant research on ZnO thin films.[67] Moreover, the well-established correlation between the voltage loss "E_g-$QFLS_{1sun}$", also denoted as voltage deficit, and Urbach energy[68,69] highlights the critical importance of minimizing the Urbach energy as much as possible. Regarding the relationship between Urbach energy and bandgap, theoretical simulations of Liu et al.[58] on $FAPb(Br_xI_{1-x})_3$ have shown that the rate of increase in Urbach energy with anion ratio evolution, and therefore bandgap, depends on the band alignment of the pure species, in their work $FAPbBr_3$ and $FAPbI_3$, and in our $FAPbBr_3$ and $FAPbCl_3$. According to the work of Liu et al., the fully linear behavior of E_u versus chlorine content, and again with bandgap, that we report in the range x_{Cl} = 0 to 0.25 would imply that the conduction band minimum of both species are fully aligned and the offset is entirely reported on valence band maximum. The work of Singh et al.[44] also reports the linear relationship between bandgap and Urbach energy, with a slope depending on the chemical phase of the compound.

The bandgap, Urbach energy and voltage loss appear to constitute the vertices of a triangle where each parameter is correlated to the two others. The primary causality, including the significant effect of the excitonic absorption in these wide-bandgap materials, is not yet fully disentangled.

4. Conclusion

In conclusion, we conducted a detailed analysis of the impact of chlorine incorporation into wide-band gap perovskite $FAPbBr_3$ thin films. Both experimental and theoretical investigations provide substantial evidence that chlorine atoms replace bromine atoms within the lattice structure, consequently inducing a pronounced change in lattice parameter, which depends closely on the localization of the chlorine in the lattice. As a consequence, the optical properties of the materials evolve as a function of the chlorine content. Notably, the introduction of chlorine leads to an increase in non-radiative losses within the absorber. These findings suggest that mixed compositions exceeding x_{Cl} = 0.19 are less promising for the development of efficient solar cells. Nevertheless, our study offers significant insights for the design of BIPV. Indeed, we demonstrate that the optimal compromise between morphology, transparency and voltage losses can be achieved with a wide band gap bromine perovskite having a chlorine content of 14%. Finally, the in-depth characterization of wide band gap perovskite materials, which includes detailed information on absorption properties, electronic structure and ultrafast recombination dynamics, has provided valuable insights into their fundamental properties. This knowledge serves as a crucial foundation for the design and optimization of various optoelectronic devices such as detectors, LEDs, or lasers, offering the potential for enhanced efficiency and performance in next-generation technologies.

5. Experimental Section

Samples Fabrication: Stock perovskite solutions of $FAPbBr_3$ and $FAPbCl_3$ were prepared by mixing the perovskite precursors (FABr, $PbBr_2$, FACl, $PbCl_2$) at a molar concentration of 1.4 M in DMSO solvent. The $FAPb(Br_{(1-x)}Cl_x)_3$ perovskite solutions were obtained by mixing the stock solutions at different volume ratios (v/v%) equal to 1:0, 1:0.14, 1:0.19, 1:0.25. The resulting perovskite films with general $FAPb(Br_{(1-x)}Cl_x)_3$ formula where the chloride/bromide molar ratio x_{Cl} was equal to 0, 0.04, 0.13, 0.20 and 0.25. The perovskite deposition was performed in a nitrogen glove box by spin coating on glass 25 mm x 25 mm and a thickness of 1 mm of the prepared solution at 4000 rpm for 20 s. Then, 200 µl of ethyl acetate used as an anti-solvent was dropped 10 s before the end of the spin coating step. Furthermore, the samples were annealed at 80 °C for 5 min.

Femtosecond Transient Absorption Spectroscopy: Femtosecond transient absorption spectroscopy (FTAS) measurements were performed using an amplified femtosecond laser system (35 fs pulse duration, 1 kHz repetition rate, 4 W power centered at 800 nm) that generates the tunable pump pulses by means of an optical parametric amplifier. The probe was a white light supercontinuum beam (360–780 nm) generated by focusing 3 µJ of the 800 nm pulse into a rotating CaF_2 crystal. The pump and the probe beams were focused on the sample with a diameter of 200 µm and 150 µm, respectively. The delay time between the two was changed by modifying the optical path of the probe, resulting in an instrument response function of 50 fs. More details can be found elsewhere.[70,71]

X-Ray Diffraction: Diffraction measurements (XRD) were performed in the Bragg-Brentano configuration by means of a Panalytical Empyrean X-ray diffractometer. A PixCel 3D detector working in linear mode accomplished the detection and a Cu-anode X-ray tube (K-Alpha1 [Å] = 1,54060; K-Alpha2 [Å] = 1,54443) was used as an impinging source. The incident optical pathway was set by divergent slits (Divergence Slit Type Fixed, Divergence Slit Size [°] = 0,2177) and patterns were collected in the $7° < 2\theta < 70°$ angular range (Gonio acquisition, Step Size [°2θ] = 0,0260, Scan Step Time [s] = 1145, Scan Type Continuous). Samples were located onto a flat sample holder for thin films and generator parameters were kept fixed at 45 mA and 40kV.

Atomic Force Microscopy: An in-house developed atomic force microscope (AFM), mounting a 30µm*30 µm scanner was used to investigate the morphological surface characteristics of the samples. A motorized system allowed for several portions of the samples to be monitored in non-contact mode by means of aluminum-coated standard tapping AFM probes (Nanosensors). Images ranging from 30*30 to 5*5 µm (500 points/image) were collected.

Photoemission Spectroscopy: Synchrotron radiation PES spectra were collected in the 35–750 eV photon energy range at the VUV-Photoemission beamline (Elettra, Trieste) under ultra-high vacuum conditions ($\approx 10^{-10}$ mbar) and at the temperature of 20 °C. The samples were measured both as-received (i.e., exposed to air) and after 6 min Ar^+ ion sputtering (500 eV ion energy, 10^{-6} A ion current on the sample) to remove air contamination from the surface. In order to minimize the effects of photon beam damage, every single spectrum was acquired on a fresh spot of the sample.

Core level spectra (Figure 2a,b; Figures S9–S11, Supporting Information) were acquired at 750 eV photon energy and fitted with Voigt functions

and Shirley baseline. The valence band spectra were acquired with photon energies in the range 35–75 eV, to derive the valence band maximum (Figure 2c) and investigate how Pb, Br and Cl atomic contributions affect the shape and branching ratio of the first three valence band states P1-P3 (Figure 2d; Figures S12–S14,S16, Supporting Information). Total electron yield was used to determine the Br 3d threshold in the photon energy range of 65–75 eV with an energy step of 0.2 eV (Figure S14, Supporting Information).

UV–VIS Spectroscopy: Reflection and transmission spectra were acquired using a Cary 5000 UV–VIS–NIR spectrophotometer from Agilent Technologies. The absorption coefficient was calculated from R and T data using the following formula (1), where "d" stands for the thickness of the perovskite layer.

$$\alpha = -\frac{1}{d} ln\left(\frac{T}{1-R}\right) \tag{8}$$

For comparison, the absorption coefficient was also calculated by fitting for each wavelength a transfer-matrix-like method taking into account all layer's Fresnel coefficients. The results were very similar and give confidence in the absorption data.

Photoluminescence Hyperspectral Imaging: The hyperspectral imaging system records a luminescence intensity signal along three sions $\{x,y,\lambda\}$. The set-up was composed of a home-built microscope with Thorlabs optomechanical elements, a 2D bandpass filtering system from company Photon Etc with 2 nm resolution, and a 4Mpix silicon-based Cmos camera Hamamatsu Orca Flash v4. The samples were illuminated ($\lambda = 405$ nm) through an infinity-corrected ×10 Olympus objective with a numerical aperture of 0.25, and the luminescence was collected through the same objective. The excitation beam and luminescence signals were separated with appropriate Thorlabs dichroic beam splitter (DMLP425) and Semrock spectral filter filters (short pass 424 nm and long pass 430 nm cut-off wavelength). The 2D luminescence signal was corrected for each pixel of the sensor from the spectral transmissions along all the optical paths, from the read noise and dark current noise of the camera. All the acquisitions were performed in the air. The incident photon flux measured was 155 mW cm^{-2} and QFLS were corrected to match 1 sun equivalent illumination.

The absorbance A is modeled as follows, E is the photon energy, E_g^* the energy of the optical transition involved in the photon absorption process, and E_u the Urbach energy:

$$A(E) = \frac{1}{1 + exp\left(-\frac{E-E_g^*}{E_u}\right)} \tag{9}$$

Post-treatment of the data cubes consists of fitting the generalized Planck law according to Equations (4) and (5) which is realized with a dedicated Matlab routine employing a least-square method algorithm. Mean spectra were fitted 100 times with random initial guess and the result set with minimum residual was selected. Fit pixel by pixel to produce maps conducted with one fit per pixel for computing speed reasons and with the same initial guess to not introduce additional variability.

Absorption Coefficient Curves Fitting for Exciton Characterization (Elliott Model): We conducted the fitting in two steps for each chlorine composition. First, we run a large number of calculations (>300) with random initial guesses and lower and upper bounds for all fitting parameters R_{exc}, E_g, σ_{ex}, σ_{cont}, A_{exc}, A_{cont}, b. We plotted the error of each simulation as a function of R_{exc}. The data points can be fitted by a quadratic curve with good accuracy whose minimum corresponds to the best solution for R_{exc}. In the second step, we conducted again all simulations (100 iterations) by setting R_{exc} fixed at the best determined value. The best dataset was defined as the median value of all solutions calculated, and all histograms were checked to ensure their low dispersion.

Density Functional Theory (DFT) Calculation: First-principles calculations have been performed with the use of the CRYSTAL code[72,73] to study the structural, electronic, and dynamic properties of the halide perovskites. This program enables us to solve both the Hartree–Fock (HF) and the Kohn–Sham (KS) systems of equations, as well as to combine them within a hybrid scheme.

As regards the atomic basis sets, all-electron GTFs have been used for H,[74] C,[74,75] N[76,77] and Cl[78] while the Stuttgart-Dresden fully relativistic pseudopotentials have been adopted for Br,[79] [8] I[80] and Pb.[81] The–3s, 3p, 3d, 4s and 4p – electrons of Br, – 4s, 4p, 4d, 5s and 5p – electrons of I and the – 5s, 5p, 5d, 6s and 6p – electrons of Pb were treated as valence electrons. The basis sets of Cl, Br, I and Pb were described in detail in Ref. [82] and the other ones in https://www.crystal.unito.it/basis_sets.

For the evaluation of the Coulomb and exchange series within CRYSTAL, the truncation thresholds for the bielectronic integrals, as defined in the CRYSTAL manual,[73] were set to 10^{-8}, 10^{-8}, 10^{-8}, 10^{-8} and 10^{-16} Ha. The calculations have been performed with $10 \times 10 \times 10$ Monkhorst-Pack k-points meshes.[33] The convergence criteria on total energies (and for the frequency determination) were 10^{-9} (10^{-12}) Ha. The atomic displacement threshold in the atomic relaxation was set to $1.8 \cdot 10^{-3}$ Bohr, and that for (converged) forces – to $4.5 \cdot 10^{-4}$ Ha/Bohr. With these computational conditions, the obtained data can be considered fully converged.

For $FAPb(Br/Cl)_3$, the Hamiltonian combines 5.625% of exact exchange from Hartree-Fock with PBE exchange-correlation functional.[29] For an accurate determination of the density of states and band structure, the spin-orbit coupling (SOC) was taken into account: the well-established underestimation of the band gap due to the SOC effect was offset by an increase in the percentage of the Hartree-Fock exact exchange to 24%. To explore the effects of the different concentrations of bromine substitution by chlorine on the perovskite properties, the same supercell approach as in Ref. [83] was used.

Supporting Information

Supporting Information is available from the Wiley Online Library or from the author.

Acknowledgements

D.O. and G.A. contributed equally to this work. The authors acknowledge the European Project "Energy Harvesting in Cities with Transparent and Highly Efficient Window-Integrated Multi-Junction Solar Cells" (CITYSOLAR) for supporting the work, which received funding from the European Union's Horizon2020 research and innovation program under grant agreement number 101007084. The authors are grateful to Mr. Marco Guaragno for the technical support in performing the XRD measurements and Dr. Daniel Suchet for his advice regarding the exciton absorption modeling. The authors acknowledge EUROFEL-ROADMAP ESFRI of the Italian Ministry of University and Research. The authors acknowledge Elettra Sincrotrone Trieste for providing access to its synchrotron radiation facilities and for financial support under the SUI internal project (proposal number 20210416).

Conflict of Interest

The authors declare no conflict of interest.

Data Availability Statement

The data that support the findings of this study are available from the corresponding author upon reasonable request.

Keywords

building-integrated photovoltaics, halide perovskites, non-radiative losses, optical properties, wide bandgap

Received: June 21, 2024
Revised: October 10, 2024
Published online:

[1] N. J. Jeon, J. H. Noh, W. S. Yang, Y. C. Kim, S. Ryu, J. Seo, S. I. Seok, *Nature* **2015**, *517*, 476.
[2] J. Dagar, M. Fenske, A. Al-Ashouri, C. Schultz, B. Li, H. Köbler, R. Munir, G. Parmasivam, J. Li, I. Levine, A. Merdasa, L. Kegelmann, H. Näsström, J. A. Marquez, T. Unold, D. M. Többens, R. Schlatmann, B. Stegemann, A. Abate, S. Albrecht, E. Unger, *ACS Appl. Mater. Interfaces* **2021**, *13*, 13022.
[3] E. L. Unger, L. Kegelmann, K. Suchan, D. Sörell, L. Korte, S. Albrecht, *J. Mater. Chem. A Mater. Energy Sustain.* **2017**, *5*, 11401.
[4] G. E. Eperon, T. Leijtens, K. A. Bush, R. Prasanna, T. Green, J. T.-W. Wang, D. P. McMeekin, G. Volonakis, R. L. Milot, R. May, A. Palmstrom, D. J. Slotcavage, R. A. Belisle, J. B. Patel, E. S. Parrott, R. J. Sutton, W. Ma, F. Moghadam, B. Conings, A. Babayigit, H.-G. Boyen, S. Bent, F. Giustino, L. M. Herz, M. B. Johnston, M. D. McGehee, H. J. Snaith, *Science* **2016**, *354*, 861.
[5] E. Aydin, E. Ugur, B. K. Yildirim, T. G. Allen, P. Dally, A. Razzaq, F. Cao, L. Xu, B. Vishal, A. Yazmaciyan, A. A. Said, S. Zhumagali, R. Azmi, M. Babics, A. Fell, C. Xiao, S. D. Wolf, *Nature* **2023**, *623*, 732.
[6] H. Dong, C. Zhang, X. Liu, J. Yao, Y. S. Zhao, *Chem. Soc. Rev.* **2020**, *49*, 951.
[7] B. Lee, T. Hwang, S. Lee, B. Shin, B. Park, *Sci. Rep.* **2019**, *9*, 4803.
[8] L. Fan, Y. Ding, J. Luo, B. Shi, X. Yao, C. Wei, D. Zhang, G. Wang, Y. Sheng, Y. Chen, A. Hagfeldt, Y. Zhao, X. Zhang, *J. Mater. Chem. A Mater. Energy Sustain.* **2017**, *5*, 7423.
[9] M. Al Katrib, E. Planes, L. Perrin, *Chem. Mater.* **2022**, *34*, 2218.
[10] Q. Chen, H. Zhou, Y. Fang, A. Z. Stieg, T.-B. Song, H.-H. Wang, X. Xu, Y. Liu, S. Lu, J. You, P. Sun, J. McKay, M. S. Goorsky, Y. Yang, *Nat. Commun.* **2015**, *6*, 7269.
[11] B. Suarez, V. Gonzalez-Pedro, T. S. Ripolles, R. S. Sanchez, L. Otero, I. Mora-Sero, *J. Phys. Chem. Lett.* **2014**, *5*, 1628.
[12] S. D. Stranks, G. E. Eperon, G. Grancini, C. Menelaou, M. J. P. Alcocer, T. Leijtens, L. M. Herz, A. Petrozza, H. J. Snaith, *Science* **2013**, *342*, 341.
[13] S. Bernard, S. Jutteau, S. Mejaouri, S. Cacovich, I. Zimmermann, A. Yaiche, S. Gbegnon, D. Loisnard, S. Collin, A. Duchatelet, F. Sauvage, J. Rousset, *Sol. RRL* **2021**, *5*, 2100391.
[14] V. Larini, M. Degani, G. Pica, C. Ding, Z. Andaji-Garmaroudi, F. Faini, S. D. Stranks, C.-Q. Ma, G. Grancini, *Sol. RRL* **2022**, *6*, 2200038.
[15] M. Mateen, Z. Arain, Y. Yang, X. Liu, S. Ma, C. Liu, Y. Ding, X. Ding, M. Cai, S. Dai, *ACS Appl. Mater. Interfaces* **2020**, *12*, 10535.
[16] C. A. Aranda, A. O. Alvarez, V. S. Chivrony, C. Das, M. Rai, M. Saliba, *Joule* **2024**, *8*, 241.
[17] W. Zia, M. Malekshahi Byranvand, T. Rudolph, M. Rai, M. Kot, C. Das, M. Kedia, M. Zohdi, W. Zuo, V. Yeddu, M. I. Saidaminov, J. I. Flege, T. Kirchartz, M. Saliba, *ACS Energy Lett.* **2024**, *9*, 1017.
[18] D. Di Girolamo, G. Vidon, J. Barichello, F. Di Giacomo, F. Jafarzadeh, B. Paci, A. Generosi, M. Kim, L. A. Castriotta, M. Frégnaux, J.-F. Guillemoles, F. Brunetti, P. Schulz, D. Ory, S. Cacovich, A. Di Carlo, F. Matteocci, *Adv. Energy Mater.* **2024**, 2400663.
[19] F. Jafarzadeh, L. A. Castriotta, M. Legrand, D. Ory, S. Cacovich, Z. Skafi, J. Barichello, F. De Rossi, F. Di Giacomo, A. Di Carlo, T. Brown, F. Brunetti, F. Matteocci, *ACS Appl. Mater. Interfaces* **2024**, *16*, 17607.
[20] A. Sadhanala, S. Ahmad, B. Zhao, N. Giesbrecht, P. M. Pearce, F. Deschler, R. L. Z. Hoye, K. C. Gödel, T. Bein, P. Docampo, S. E. Dutton, M. F. L. De Volder, R. H. Friend, *Nano Lett.* **2015**, *9*, 6101.
[21] F.-X. Liang, S.-F. Li, J. Yu, L.-L. Zhou, J. Wang, C. Fu, X. An, J.-A. Huang, L. Wang, L.-B. Luo, *J. Mater. Chem.* **2023**, *11*, 10198.
[22] Q. Zhang, X. Liu, X. Zhang, Z. Wang, B. Zhang, Y. Hao, A. Dubois, W. Jie, Y. Xu, *J. Mater. Chem. A Mater. Energy Sustain.* **2024**, *12*, 3304.
[23] R. Comin, G. Walters, E. S. Thibau, O. Voznyy, Z.-H. Lu, E. H. Sargent, *J. Mater. Chem.* **2015**, *3*, 8839.
[24] N. Rybin, D. Ghosh, J. Tisdale, S. Shrestha, M. Yoho, D. Vo, J. Even, C. Katan, W. Nie, A. J. Neukirch, S. Tretiak, *Chem. Mater.* **2020**, *32*, 1854.
[25] J. Hieulle, X. Wang, C. Stecker, D.-Y. Son, L. Qiu, R. Ohmann, L. K. Ono, A. Mugarza, Y. Yan, Y. Qi, *J. Am. Chem. Soc.* **2019**, *141*, 3515.
[26] F. Matteocci, D. Rossi, L. A. Castriotta, D. Ory, S. Mejaouri, M. A. der Maur, F. Sauvage, S. Cacovich, A. D. Carlo, *Nano Energy* **2022**, *101*, 107560.
[27] G. Mannino, I. Deretzis, E. Smecca, F. Giannazzo, S. Valastro, G. Fisicaro, A. La Magna, D. Ceratti, A. Alberti, *J. Phys. Chem. C* **2021**, *125*, 4938.
[28] L. Wang, K. Wang, B. Zou, *J. Phys. Chem. Lett.* **2016**, *7*, 2556.
[29] A. Oranskaia, J. Yin, O. M. Bakr, J.-L. Brédas, O. F. Mohammed, *J. Phys. Chem. Lett.* **2018**, *9*, 5474.
[30] V. Milotti, S. Cacovich, D. R. Ceratti, D. Ory, J. Barichello, F. Matteocci, A. Di Carlo, P. M. Sheverdyaeva, P. Schulz, P. Moras, *Small Methods* **2023**, *7*, 2300222.
[31] H. Wu, Y. Ge, G. Niu, J. Tang, *Matter* **2021**, *4*, 144.
[32] A. W. Y. Ho-Baillie, H. G. J. Sullivan, T. A. Bannerman, H. P. Talathi, J. Bing, S. Tang, A. Xu, D. Bhattacharyya, I. H. Cairns, D. R. McKenzie, *Adv. Mater. Technol.* **2022**, *7*, 2101059.
[33] A. Franz, D. M. Többens, F. Lehmann, M. Kärgell, S. Schorr, *Acta Crystallogr B Struct Sci Cryst Eng Mater* **2020**, *76*, 267.
[34] J. P. Perdew, A. Ruzsinszky, G. I. Csonka, O. A. Vydrov, G. E. Scuseria, L. A. Constantin, X. Zhou, K. Burke, *Phys. Rev. Lett.* **2008**, *100*, 136406.
[35] D. Gill, P. Bhumla, P. Basera, S. Bhattacharya, *J. Phys. D Appl. Phys.* **2021**, *4*, 025005.
[36] D. E. Parry, *Rapid Commun. Mass Spectrom.* **1994**, *8*, 579.
[37] S. Cacovich, P. Dally, G. Vidon, M. Legrand, S. Gbegnon, J. Rousset, J.-B. Puel, J.-F. Guillemoles, P. Schulz, M. Bouttemy, A. Etcheberry, *ACS Appl. Mater. Interfaces* **2022**, *14*, 34228.
[38] J. Endres, D. A. Egger, M. Kulbak, R. A. Kerner, L. Zhao, S. H. Silver, G. Hodes, B. P. Rand, D. Cahen, L. Kronik, A. Kahn, *J. Phys. Chem. Lett.* **2016**, *7*, 2722.
[39] N. Lynn, L. Mohanty, S. Wittkopf, *Build. Environ.* **2012**, *54*, 148.
[40] A. Ghosh, P. Selvaraj, S. Sundaram, T. K. Mallick, *Sol. Energy* **2018**, *163*, 537.
[41] R. J. Elliott, *Phys. Rev.* **1957**, *108*, 1384.
[42] X. Chen, H. Lu, Y. Yang, M. C. Beard, *J. Phys. Chem. Lett.* **2018**, *9*, 2595.
[43] D. D. Sell, P. Lawaetz, *Phys. Rev. Lett.* **1971**, *26*, 311.
[44] S. Singh, C. Li, F. Panzer, K. L. Narasimhan, A. Graeser, T. P. Gujar, A. Köhler, M. Thelakkat, S. Huettner, D. Kabra, *J. Phys. Chem. Lett.* **2016**, *7*, 3014.
[45] M. Saba, F. Quochi, A. Mura, G. Bongiovanni, *Acc. Chem. Res.* **2016**, *49*, 166.
[46] Y. Yang, M. Yang, K. Zhu, J. C. Johnson, J. J. Berry, J. van de Lagemaat, M. C. Beard, *Nat. Commun.* **2016**, *7*, 12613.
[47] F. Ruf, M. F. Aygüler, N. Giesbrecht, B. Rendenbach, A. Magin, P. Docampo, H. Kalt, M. Hetterich, *APL Mater.* **2019**, *7*, 031113.
[48] J. Shi, H. Zhang, Y. Li, J. J. Jasieniak, Y. Li, H. Wu, Y. Luo, D. Li, Q. Meng, *Energy Environ. Sci.* **2018**, *11*, 1460.
[49] C. L. Davies, M. R. Filip, J. B. Patel, T. W. Crothers, C. Verdi, A. D. Wright, R. L. Milot, F. Giustino, M. B. Johnston, L. M. Herz, *Nat. Commun.* **2018**, *9*, 293.
[50] D. M. Niedzwiedzki, H. Zhou, P. Biswas, *J. Phys. Chem. C* **2022**, *126*, 1046.
[51] K. Galkowski, A. Mitioglu, A. Miyata, P. Plochocka, O. Portugall, G. E. Eperon, J. T.-W. Wang, T. Stergiopoulos, S. D. Stranks, H. J. Snaith, R. J. Nicholas, *Energy Environ. Sci.* **2016**, *9*, 962.

[52] X. Geng, Y. Liu, X. Zou, E. M. J. Johansson, J. Sá, *J. Phys. Chem. C* **2023**, *127*, 3085.
[53] P. F. Ndione, Z. Li, K. Zhu, *J. Mater. Chem.* **2016**, *4*, 7775.
[54] M. Jain, D. Gill, P. Bhumla, P. Basera, S. Bhattacharya, *Appl. Phys. Lett.* **2021**, *118*, 192103.
[55] G. Lasher, F. Stern, *Phys. Rev.* **1964**, *133*, A553.
[56] P. Wurfel, *J. Phys.* **1982**, *15*, 3967.
[57] W. van Roosbroeck, W. Shockley, *Phys. Rev.* **1954**, *94*, 1558.
[58] Y. Liu, J.-P. Banon, K. Frohna, Y.-H. Chiang, G. Tumen-Ulzii, S. D. Stranks, M. Filoche, R. H. Friend, *ACS Energy Lett.* **2023**, *8*, 250.
[59] J. S. Manser, P. V. Kamat, *Nat. Photonics* **2014**, *8*, 737.
[60] W. Rehman, R. L. Milot, G. E. Eperon, C. Wehrenfennig, J. L. Boland, H. J. Snaith, M. B. Johnston, L. M. Herz, *Adv. Mater.* **2015**, *27*, 7938.
[61] E. Mosconi, A. Amat, M. K. Nazeeruddin, M. Grätzel, F. De Angelis, *J. Phys. Chem. C* **2013**, *117*, 13902.
[62] G. Ammirati, F. Martelli, P. O'Keeffe, S. Turchini, A. Paladini, M. Palummo, G. Giorgi, M. Cinquino, M. De Giorgi, L. De Marco, D. Catone, *Adv. Opt. Mater.* **2023**, *11*, 2201874.
[63] G. Mannino, I. Deretzis, E. Smecca, A. La Magna, A. Alberti, D. Ceratti, D. Cahen, *J. Phys. Chem. Lett.* **2020**, *11*, 2490.
[64] M. Feng, S. Ye, Y. Guo, T. C. Sum, *Nano Lett.* **2022**, *22*, 7195.
[65] M. Li, P. Huang, H. Zhong, *J. Phys. Chem. Lett.* **2023**, *14*, 1592.
[66] M. P. U. Haris, S. Kazim, S. Ahmad, *ACS Appl. Mater. Interfaces* **2022**, *14*, 24546.
[67] D. Dimova-Malinovska, H. Nichev, O. Angelov, *Phys. Status Solidi C* **2008**, *5*, 3353.
[68] B. Subedi, C. Li, C. Chen, D. Liu, M. M. Junda, Z. Song, Y. Yan, N. J. Podraza, *ACS Appl. Mater. Interfaces* **2022**, *14*, 7796.
[69] J. Chantana, Y. Kawano, T. Nishimura, A. Mavlonov, T. Minemoto, *Sol. Energy Mater. Sol. Cells* **2020**, *210*, 110502.
[70] J. S. Pelli Cresi, L. Di Mario, D. Catone, F. Martelli, A. Paladini, S. Turchini, S. D'Addato, P. Luches, P. O'Keeffe, *J. Phys. Chem. Lett.* **2020**, *11*, 5686.
[71] D. Catone, L. Di Mario, F. Martelli, P. O'Keeffe, A. Paladini, J. Stefano Pelli Cresi, A. K. Sivan, L. Tian, F. Toschi, S. Turchini, *Nanotechnology* **2020**, *32*, 025703.
[72] A. Erba, J. K. Desmarais, S. Casassa, B. Civalleri, L. Donà, I. J. Bush, B. Searle, L. Maschio, L. Edith-Daga, A. Cossard, C. Ribaldone, E. Ascrizzi, N. L. Marana, J.-P. Flament, B. Kirtman, *J. Chem. Theory Comput.* **2023**, *19*, 6891.
[73] R. Dovesi, R. Orlando, A. Erba, C. M. Zicovich-Wilson, *Int. J. Quantum Chem.*.
[74] C. Lechner, P. Baranek, H. Vach, *Carbon N. Y.* **2018**, *127*, 437.
[75] C. Lechner, B. Pannier, P. Baranek, N. C. Forero-Martinez, H. Vach, *J. Phys. Chem. C Nanomater. Interfaces* **2016**, *120*, 5083.
[76] C. Gatti, V. R. Saunders, C. Roetti, *J. Chem. Phys.* **1994**, *101*, 10686.
[77] M. A. Spackman, A. S. Mitchell, *Phys. Chem. Chem. Phys.* **2001**, *3*, 1518.
[78] E. Apra, M. Causa, M. Prencipe, R. Dovesi, V. R. Saunders, *J. Phys. Condens. Matter* **1993**, *5*, 2969.
[79] K. A. Peterson, D. Figgen, E. Goll, H. Stoll, M. Dolg, *J. Chem. Phys.* **2003**, *119*, 11113 .
[80] K. A. Peterson, B. C. Shepler, D. Figgen, H. Stoll, *J. Phys. Chem. A.* **2006**, *110*, 13877.
[81] B. Metz, H. Stoll, M. Dolg, *J. Chem. Phys.* **2000**, *113*, 2563.
[82] A. Mishra, P. Baranek, A. Postnikov, *Surf. Interfaces* **2021**, *25*, 101264.
[83] F. Lafond, P. Baranek, A. Postnikov, *J. Phys. Chem. C* **2020**, *124*, 10353.